



CT/MR-Compatible Physical Human-Robotized Needle Interactions: from Modeling to Percutaneous Steering

Ederson Antônio Gomes Dorileô, Nabil Zemiti, Sébastien Krut, Philippe Poignet

► To cite this version:

Ederson Antônio Gomes Dorileô, Nabil Zemiti, Sébastien Krut, Philippe Poignet. CT/MR-Compatible Physical Human-Robotized Needle Interactions: from Modeling to Percutaneous Steering. Mechatronics, 2022, 85, pp.102840. 10.1016/j.mechatronics.2022.102840 . lirmm-03680857

HAL Id: lirmm-03680857

<https://hal-lirmm.ccsd.cnrs.fr/lirmm-03680857>

Submitted on 29 May 2022

HAL is a multi-disciplinary open access archive for the deposit and dissemination of scientific research documents, whether they are published or not. The documents may come from teaching and research institutions in France or abroad, or from public or private research centers.

L'archive ouverte pluridisciplinaire **HAL**, est destinée au dépôt et à la diffusion de documents scientifiques de niveau recherche, publiés ou non, émanant des établissements d'enseignement et de recherche français ou étrangers, des laboratoires publics ou privés.

CT/MR-Compatible Physical Human-Robotized Needle Interactions: from Modeling to Percutaneous Steering

derson DORILEO, Nabil ZEMITI*, Sbastien KRUT, and Philippe POIGNET

LIRMM, University Montpellier, CNRS, Montpellier, France^{1,*}

Abstract

In recent years a number of robotic steering systems have been proposed that are geared towards improving interventional radiology procedures such as tumor ablation and biopsy. These solutions have introduced new safety challenges in the physical human-robot interaction domain. This study presents a new 3D robotized needle steering algorithm compatible with CT and MR-imaging guidance. The steering algorithm is featured with an adaptive self-correction mechanism that works as a failure contingency tool that could be adapted online at each insertion step. The developed pHRI solution was designed to be compatible to ferro-magnetic issues and a reduced workspace inside the scanner bore. As far as we know, this is the first approach designed to steer rigid needles free of force sensors and which meets the challenges that prevail in our context. Our proposed approach helps overcome safety issues regarding the physical interaction between robotized needles and patients. Validation testing highlighted the feasibility of the new needle steering algorithm, while its accuracy revealed the potential of the approach under the proposed scope of application.

Keywords: pHRI, Needle steering, Robotized needles, CT/MRI-compatible, Percutaneous insertion, Rigid needles, Interventional Radiology.

1. Introduction

Interventional radiology (IR), involving radiological image guidance, is a minimally-invasive alternative to open surgery. Image-guided percutaneous needle placement interventions through multilayered soft tissues are now widely used in abdominopelvic care procedures such as biopsy, aspiration, drug delivery and tumor ablation. For such clinical procedures, Computed Tomography (CT) and magnetic resonance imaging (MRI) are important standards to guide the radiologists. However, CT and MRI-guided IR may be problematic for interventional radiologists because of the constrained bore space and safety constraints (radiation exposure and high magnetic fields for CT and MRI, respectively). To tackle clinical challenges that may arise in IR and assist radiologists in their operations, convergent research in areas such as physical human-robot cooperation, including robot design, sensing, modeling, manipulation and autonomy, has been under way to enable highly flexible and versatile medical robots, with enhanced capabilities to feel, touch and decide [1]. Different robotized needle solutions with embedded sensing capabilities have been proposed in the literature to improve the accuracy and safety of IR procedures [2], [3], [4]. However, robotized needle manipulation by radiologists as well as insertion and steering inside the patients soft tissue has given rise to new safety challenges in the physical

human-robot interaction domain. Indeed, robotized needles interact distally (tip and shaft) with the patient and proximally (needle base) with the radiologist through remote manipulation (teleoperation) [5] or comanipulation [6]. Consequently, safety issues regarding the physical interaction between robotized needles and patients need to be tackled. Even more, if the robotized needle is comanipulated by the radiologist, this introduces a second challenge regarding pHRI safety, but it is out of the scope of the paper.

In the IR domain, robot design, sensing and modeling are critical for planning and performing safe pHRI under CT and MRI-guidance [1], [7], [8]. To date, only a few MR-compatible robots [9], [10], [3], [4] have been designed that are able to perform translation, rotation, and insertion of long (≈ 20 cm) needles under abdominopelvic procedures. However, solutions proposed in the literature for sensing and modeling for robotized needle steering are usually dependent on metallic force sensors [11], [12], [13], [14]. This hampers their clinical use, notably due to safety issues due to ferromagnetic incompatibilities with imaging modalities used. Indeed, robotized needle steering methods have put efforts in the interaction modeling of needle and multi-layered soft tissue deformations during percutaneous insertion.

Mechanics-based [15], [16] and kinematics-based [17], [13] models estimate needle tip motion based on the fundamental material, geometrical or motion properties. Numerical-based solutions [18], [19], [20] address needle-tissue deflection estimation issues, especially when mathematical models are highly complicated. However, these methods are usually based on in-

*Corresponding author

Email address: nabil.zemiti@lirmm.fr (LIRMM, University Montpellier, CNRS, Montpellier, France)

teraction force measurement and thus not compatible with the considered IR procedures.

The pHRI modeling approach proposed here is based on phenomenological model principles. Rather than being purely focused on mechanical, kinetic or kinematical analysis, phenomenological models have been used to fit experimental data to parametric models. Accurate physics is usually not deemed a priority in these models. Contrary to numerical-based solutions, which are often computationally expensive, phenomenological models have been developed to enable real-time implementation. Even so, previous studies [21], [12], [22], [23], [24] have shown that they are able to abstract system behavior with enough accuracy to be used in planning and control approaches. Although the submillimeter error results in most of the experiments presented above may serve to validate the proposed methodologies, it should be mentioned that the methods presented in many of these studies cannot be directly implemented in (3D) CT and MRI conditions. This is because of concerns related to patient safety, as well as compatibility issues regarding the use of rigid needles in nonholonomic approaches [13].

We thus devised an approach that could fill this gap. Here we extended studies presented previously [25], [26] by integrating an adaptive needle deflection model into a pHRI solution for needle steering to overcome metallic-compatibility issues. To the best of our knowledge, this is the first approach designed to steer rigid needles through multi-layered soft tissues. This approach is entirely free of force measurements and has been designed to be compatible with both CT and MRI-guided IR procedures. This contributes to answer to the safety challenges in the physical human-robot interaction domain.

Note that the study of needle-tissue interaction forces is crucial to provide robot-assisted systems with relevant information. These interactions forces generate phenomena such as needle deflection, friction, cutting forces, and tissue elastic deformation [14]. For this reason, models proposed in the literature often assume that force measurement is a standard input. Instead, skipping the use of force sensors could lead to simpler solutions by enabling the use of native CT/MR-compatible needle-steering approaches, while avoiding competition for scarce and expensive non-metallic force-input measurement solutions.

An alternative clinically sustainable solution based on visual feedback of the needle tip position is thus proposed.

Hereafter is a detailed discussion on how we designed our pHRI adaptive needle steering assistance, as well as on the potential of the approach to cope with uncertainties for different setups (robots, needles and tissues) under the proposed scope of application.

2. Materials and Methods

2.1. Adaptive Needle Deflection Modeling

Here after we present an extension of our research on adaptive modeling of rigid needle/soft tissue interactions [27] where the model was designed as a function of:

- Needle kinematic parameters: needle insertion depth δy_i and needle tip position N_i relative to the iterative time i
- Needle kinetic and biomechanical parameters: needle and tissue stiffness K_n and K_t , respectively
- Needle geometry including the needle tip asymmetry angle α .

In reference to the small deflection theory of beams where the beam length \mathcal{L} is linked to the beam deflection δx with $\delta x/\mathcal{L} < 0.1$ [28], rigid needles are assumed to deflect in the direction of the bevel due to the presence of asymmetric forces acting on the needle tip. The needle bending angle θ is thus considered to approach zero, according to the small-angle approximate, where $\sin \theta \approx \theta$ (Fig. 1).

In the Kinematic Analysis section, we build the needle deflection prediction algorithm. This allows geometrical location of the predicted needle tip position \widehat{N}_{i+1} w.r.t the current measured needle tip position N_i .

In the Kinetic Interaction Modelling section, the interaction forces causing the needle deformation are analyzed to derive the locally linear relationship between the estimated needle deflection δx_{i+1} at the depth δy_{i+1} and the needle/tissue biomechanical properties.

2.1.1. Kinematic Analysis

In conventional IR procedures, needles are usually inserted progressively, with quasi-static motion and intermediate insertion depth δy_i relative to the iterative time i . In this study, the needle and its path are modeled as articulated links, where θ_i is the deflection angle between two consecutive links. Each link length is dependent on δy_i . The needle entry point E is assumed to be fixed at this stage of modeling (see Fig. 1).

For each insertion step δy_i , the designed model predicts the corresponding deflection δx_i , *i.e.* the needle tip deflection orthogonal to the insertion direction.

Hereafter, $\widehat{\delta x}_i$ is defined as the predicted value of δx_i . We thus focused our modeling so as to only predict the needle tip position \widehat{N}_{i+1} w.r.t the current needle tip position N_i at step i . We did not consider the intermediate steps located between i and $i + 1$.

A rigid needle is defined as a beveled hollowed cylinder (cannula) having a biomechanical stiffness given by [12]:

$$K_n = 3EI/\mathcal{L}^3 \quad (1)$$

(EI) is the flexural rigidity, E is the Youngs modulus and I is the second moment of inertia. The Youngs modulus E is sensitive to the needle material (e.g. $E = 193$ GPa for a stainless (316) steel needle). The second moment of inertia I for a hollowed cylinder having an outer diameter d_{out} and an inner diameter d_{inn} , is given by:

$$I = \frac{\pi}{64} (d_{out}^4 - d_{inn}^4) \quad (2)$$

In Eq. (1), $\mathcal{L} = \mathcal{L}_{out} + \mathcal{L}_{in}$ is the needle length projected along the y -axis (Fig. 1.III). It is related to the portion of the

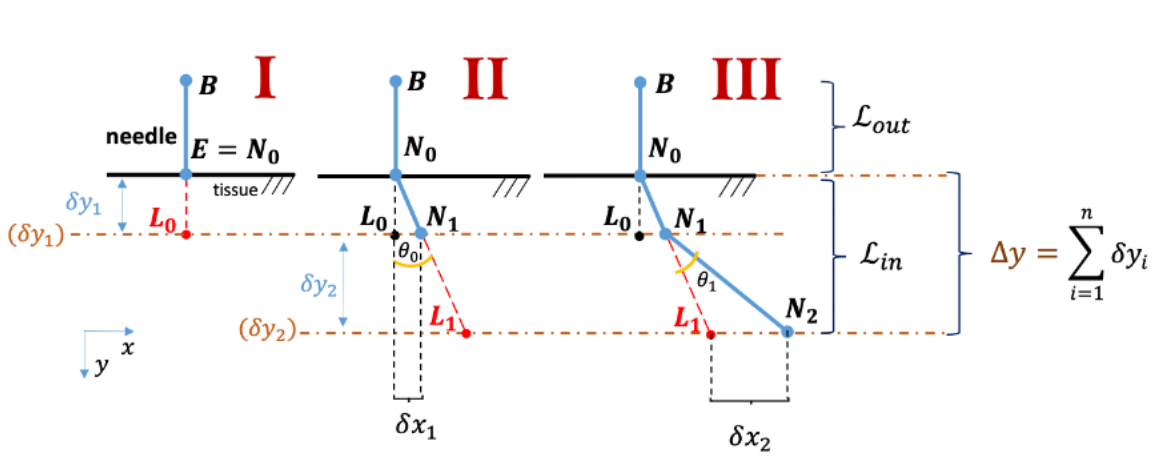


Figure 1: Illustration of the iterative needle insertion procedure (out of scale drawings showing two insertion steps $i = 0, 1, 2$). The deflection of the needle tip δx_{i+1} is defined as the distance between the points L_i and N_{i+1} at the level of (δy_{i+1})

needle length that is below the robot end-effector, and is therefore under the action of the input force. \mathcal{L}_{out} is the $[BE]$ segment of the needle between the robot end-effector B and the tissue entry point E . Consequently, \mathcal{L}_{out} is always outside the soft tissue, while \mathcal{L}_{in} is located inside the tissue along the y -axis. Note that during the insertion procedure, some robots perform a peristaltic-like incremental needle insertion using gripper-based end-effectors which leads to a varying \mathcal{L} value [10]. Consequently, since \mathcal{L} increases as the robot inserts the needle, the needle stiffness K_n is no longer constant and needs to be updated w.r.t. \mathcal{L} via Eq. (1).

For simplicity, in our experiments we considered tissue stiffness K_t as being constant along the insertion path (*i.e.* homogeneous tissue), according to the measurements obtained at the tissue surface. However, in the future, tissue stiffness information regarding the full insertion depth could be obtained preoperatively using MR or acoustic-based elastography imaging techniques. In such cases, the tissue stiffness K_{t_i} could be updated in the iterative model for each penetration step. This could be performed without further change in our model design, as proposed below. Moreover, for the model development, we considered that the needle only moves in a two-dimensional plane, as defined by the image slice. However, this could be easily extended to 3D scenarios if it is considered that the needle moves beyond this 2D plane, as discussed later.

2.1.2. Iterative Percutaneous Procedure

Fig. 1 shows progressive changes in the iterative insertion procedure, while considering the kinematic-based parameters, as described above. The needle tip positions N_i are described, along the current iterative time i , as a function of the insertion depth δy_i . Considering, the next insertion depth δy_{i+1} , our model can estimate the needle tip position \widehat{N}_{i+1} by calculating the incremental needle deflection δx_{i+1} relative to the line $(N_{i-1}N_i)$ as follows:

Let L_i be the point defined by the intersection between the line $(N_{i-1}N_i)$ and the horizontal line defined at the level of the

horizontal line (δy_{i+1}) . The deflection δx_{i+1} is calculated as the distance between the points L_i and N_{i+1} at the level of (δy_{i+1}) .

For instance, Fig. 1.I illustrates the situation for the initial time step $i = 0$ where the needle tip is placed at the entry point E and its tip position is given by N_0 . The point L_0 is given by the intersection between the line $(BE) = (BN_0)$ with the horizontal section line (δy_1) corresponding to the (next) insertion depth δy_1 . Then, one insertion step further ($i = 1$), the needle tip position is at N_1 while showing the measured deflection δx_1 (Fig. 1.II). δx_1 is calculated as the distance between L_0 and N_1 at the level of (δy_1) . Then, the point L_1 (Fig. 1.II) is given by the intersection between (N_0N_1) and (δy_2) . δx_2 is the distance between L_1 and N_2 at the level of (δy_2) .

Based on the estimated value of the deflection $\widehat{\delta x}_{i+1}$ (see next section), the needle tip position \widehat{N}_{i+1} could be predicted as the deviation of L_i by $\widehat{\delta x}_{i+1}$ at the level of (δy_{i+1}) . Therefore, the estimated needle tip position \widehat{N}_{i+1} can be expressed, for each insertion step by:

$$\widehat{N}_{i+1} = L_i + \begin{bmatrix} \widehat{\delta x}_{i+1} \\ 0 \end{bmatrix} \quad (3)$$

where $L_i = N_i + \begin{bmatrix} \delta y_i \cdot \theta_{i-1} \\ \delta y_i \end{bmatrix}$

Indeed, as presented Fig. 2.I, at the initial step ($i = 0$), the predicted deflection relative to L_0 is given by $\widehat{\delta x}_1$. This allows us to calculate the predicted needle tip position \widehat{N}_1 . After the first insertion step $i = 1$ (at depth δy_1), based on the measured needle tip position N_1 , we can calculate the current needle deflection δx_1 (relative to the previous L_0 , cf. Fig. 2.II). Similarly, we can estimate the next needle position \widehat{N}_2 defined by the deviation $\widehat{\delta x}_2$ relative to L_1 while penetrating the needle to depth δy_2 . This also applies to the subsequent insertion steps.

2.1.3. Kinetic modeling

Contrary to what has been presented in [12], we modeled the needle as a concatenation of articulated rigid body segments $[N_{i-1}N_i]$, where the last segment representing the needle tip is

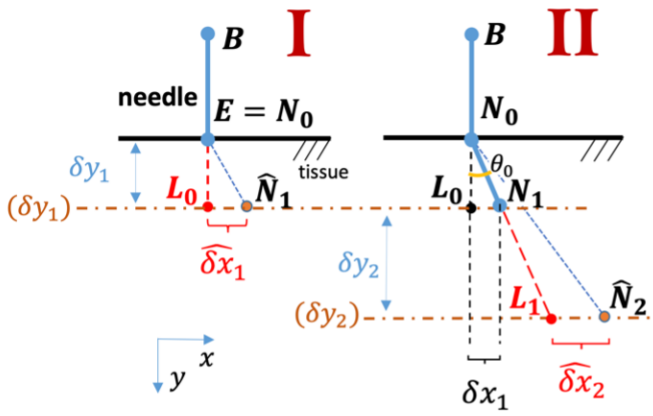


Figure 2: Out of scale drawings showing how the designed model estimates the needle tip position \hat{N}_{i+1} by calculating the incremental needle deflection $\delta\hat{x}_{i+1}$ as the deviation of L_i at the level of (δy_{i+1}) . Two insertion steps $i = 0, 1$ are considered here.

supported by an equivalent orthogonal virtual spring of stiffness K_n fixed to the needle tip Fig. 3. This stiffness represents the needle lateral deformation. We also considered that the needle is incompressible along its axis, *i.e.* its axial deformation is negligible compared to tissue deformation.

It is also assumed that the needle has a quasi-static motion and that the linear lateral interaction forces respond for small displacements. Hence, through this phenomenological analysis, the needle tip-tissue interaction forces can be modeled as a slipping motion, in the presence of friction, between two rigid bodies (needle tip and an inclined plane) both attached to virtual springs. As illustrated in Fig. 4, this inclined plane is rigidly attached to two virtual springs K_t . The latter represents the local 2D tissue stiffness. The equations given here after (Eq. (4)) are derived from this previous phenomenological analysis and relate to the needle equilibrium during insertion into soft tissue. They give the relationship between the resulting force components (R_x) and (R_y) affecting the needle tip (Fig. 3). This equilibrium is maintained at the beginning of each penetration step, but after the tissue relaxation phase. For our model validity, it is thus necessary to wait for tissue relaxation (≈ 5 s) before each new insertion step. This was the case in our study and is currently the case in clinical conditions in which sequential insertion steps are considered with MR-imaging updates between insertions.

The resulting force \mathbf{R} is the sum of all forces interacting with the system, *i.e.* mainly the input force \mathbf{F} applied on the needle base and the friction force \mathbf{F}_μ . In our study, it is assumed that the resulting force component on the x -axis R_x is equal to the force needed to compress the parallel virtual springs. The stiffness of each spring is given by the needle and the tissue stiffness (K_n and K_t resp.). The resulting y -component R_y is represented, on its side, by a single spring with stiffness K_t . This leads to:

$$R_x = (K_n + K_t) \delta x \quad (4)$$

$$R_y = K_t \delta y$$

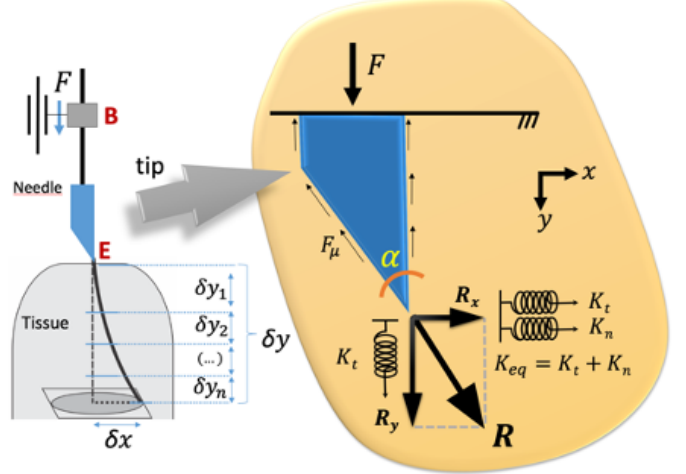


Figure 3: Modelling of the needle tip deflection. Left: Needle deflection is towards the bevel direction. Right: Resulting forces components.

Consequently, the resulting force R_x acts transversally and causes the needle deflection, while R_y is the axial force that allows needle penetration on the y -axis.

Fig. 4 illustrates the force relationship in terms of angle and cone of friction. Fig. 4.I shows the needle tip body lying on the inclined plane, where T_g and N_m are resp. the tangential and normal axes to the bevel tip. Since the needle is moving inside the tissue and thus slipping on the virtual inclined plane, the resulting force \mathbf{R} will always be located on the friction cone making an angle γ relative to the normal N_m . The friction cone [29] defines $\tan \gamma = \mu$. Fig. 4.II illustrates our study of component forces related to \mathbf{R} . Projecting the tangential and normal components (R_t and R_n resp.) of \mathbf{R} on the x and y -axes, and expressing them as a function of the friction angle γ and the needle tip angle α , gives:

$$\begin{aligned} \mathbf{R} &= \begin{bmatrix} R_x \\ R_y \end{bmatrix} = \begin{bmatrix} R_{t_x} - R_{n_x} \\ R_{t_y} + R_{n_y} \end{bmatrix} \\ &= \begin{bmatrix} R \sin \gamma \sin \alpha - R \cos \gamma \cos \alpha \\ R \sin \gamma \cos \alpha + R \cos \gamma \sin \alpha \end{bmatrix} \\ &= \begin{bmatrix} R \cos(\gamma + \alpha) \\ R \sin(\gamma + \alpha) \end{bmatrix} \end{aligned} \quad (5)$$

Where R is the norm of \mathbf{R} . Therefore,

$$\frac{R_x}{R_y} = \frac{\cos(\gamma + \alpha)}{\sin(\gamma + \alpha)} = \cot(\gamma + \alpha) \quad (6)$$

Finally, when combining Eq. (4) with Eq. (6), the needle tip deflection for the x direction can be estimated at each insertion time i as:

$$\delta\hat{x}_{i+1} = \frac{K_{t_i} \delta y_{i+1} \cot(\gamma + \alpha)}{K_{t_i} + K_{n_i}} = \frac{K_{t_i} \delta y_{i+1} H_i}{K_{t_i} + K_{n_i}} \quad (7)$$

Where $H_i = \cot(\gamma + \alpha)$ is an unknown parameter that must be estimated experimentally and adapted online, as demonstrated previously in [26]. H_i will thus be updated

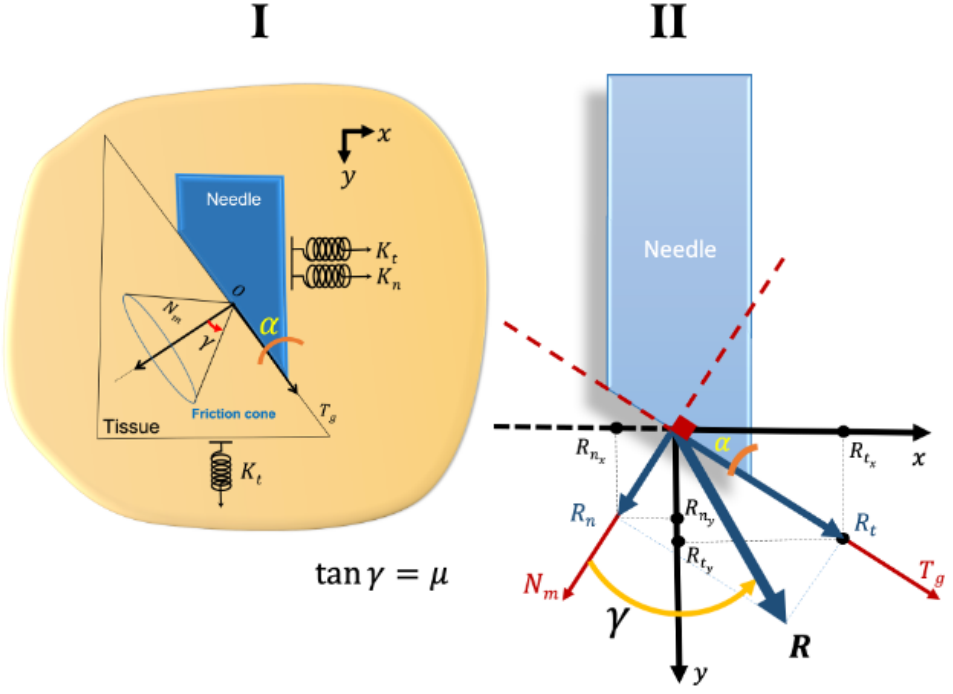


Figure 4: Study of friction cone and resulting force in the needle-tissue interaction context I. Modeling of the inclined plane assuming vertical and horizontal springs K_t , representing tissue deformation, while horizontal spring K_n represents needle deformation. II. Study of forces at the beveled needle tip with angle α .

for each insertion step w.r.t. the current needle tip position N_i . This iterative approach allows to compensate for the uncertainties related to the tissues' anisotropy and needle stiffness.

The deflection estimation $\widehat{\delta x}_{i+1}$ for the insertion depth δy_{i+1} is performed while considering the update of H_i at time i . By applying the inverse of Eq. (7) and measuring the current needle deflection δx_i , H_i is updated for each insertion step i :

$$H_i = \frac{(K_{t_i} + K_{n_i}) \delta x_i}{K_{t_i} \delta y_i} \quad (8)$$

In Eq. (8), thanks to the proposed iterative insertion process together with the rigid needle small-deflection theory, there is no need to consider the influence of the change of K_{t_i} on H_i that could be related to tissues anisotropy.

The initial value H_0 is preoperatively set using empirical data obtained from preliminary experiments [26].

2.2. Needle Steering Assistance

Fig. 5 shows lateral manipulation experiments at the proximal base $\|\mathbf{B} - \mathbf{B}'\| \approx 10$ mm while the needle has been inserted at nearly 30 mm depth.

These experiments performed under a CT-scanner allowed us to conduct the behavioral analysis of the needle-tissue interaction. They reveal non-negligible motion $\|\mathbf{E} - \mathbf{E}'\| \approx 2$ mm, at the tissue entry point, while pivoting at a point \mathbf{V} located inside the tissue close to the needle tip. They showed also negligible motion of the needle tip $\|\mathbf{N} - \mathbf{N}'\| \approx 0.4$ mm.

Therefore, based on these analyses, we could formulate the two following needle steering algorithm assumptions, as shown in Fig. 5.

First, lateral manipulation at the proximal base of the needle implies a steering angle φ_i , as defined below, thereby causing the needle to pivot at its tip N_i . Secondly, the simplest and shortest approximation for the current needle shaft position is given by the line $(\mathbf{B}_i N_i)$, where \mathbf{B}_i is the needle base at step i and N_i is the current needle tip position.

Next, lateral manipulation at the proximal base of the needle is performed to guide its tip towards a targeted point \mathbf{T} located inside the tissue at a depth Δy from the entry point \mathbf{E} .

For the needle steering strategy, our needle deflection model Eqs (3) and (7) is used to predict the final needle tip position $\widehat{\mathbf{N}}_{F_i}$ while steered by φ_i , at the level of the full insertion depth Δy , i.e. at the horizontal line where the targeted point \mathbf{T} is located (see Fig. 6). We assume that \mathbf{T} could move due to needle-tissue interactions or physiological motions, and its measured position at step i is given by \mathbf{T}_i .

Considering \mathbf{B}_{i-1} as the base position before steering and \mathbf{B}_i its current position after steering, the steering angle φ_i is defined as the (planar) incremental pivot angle around the needle tip N_i of the two intersecting lines $(\mathbf{B}_{i-1} N_i)$ and $(\mathbf{B}_i N_i)$.

At the beginning of the needle steering experiments, our needle deflection model is used to help users to define the optimal location of the tissue entry point \mathbf{E} . Assuming the full insertion depth (Δy) and no steering applied ($\varphi_0 = 0$) nor needle insertion, the needle entry point assistance involves reverse use of the deflection model (Eqs (3) and (7)). Therefore, once the current target position \mathbf{T}_0 is provided as input, it is then possible to propose the optimal entry point \mathbf{E} where the needle tip should be placed ($N_0 = \mathbf{E}$) at the beginning of the insertion (Fig. 6.I) to minimize targeting error and to get $\widehat{\mathbf{N}}_{F_0} = \mathbf{T}_0$. At this preoperative entry point assistance step, the needle tip

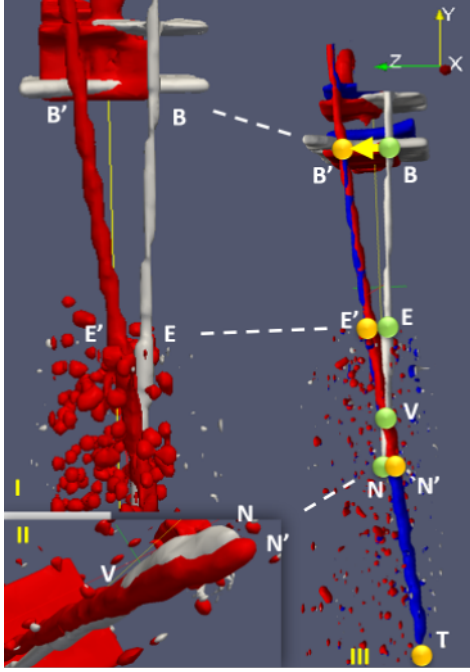


Figure 5: 3D high resolution CT reconstruction of the system. The image shows an insertion example with lateral motion of the needle base $\mathbf{B} - \mathbf{B}'$. (I) Displacement of the needle entry point $E - E'$. (II) tip $N - N'$. (III) Inserted needle towards \mathbf{T} after lateral manipulation. The simplest and fastest approximation of the needle shaft motion is given by the segment $[B'N']$.

is positioned at the tissue surface and no needle insertion nor steering are considered yet.

For steering convenience, the line $(\mathbf{B}_i\mathbf{N}_i)$ represents the current needle axis related to the steering angle φ_i . According to Fig. 6.II-III and considering the needle-tip at \mathbf{N}_i , the estimated needle tip position $\widehat{\mathbf{N}}_{F_i}$ is calculated as the deviation of the point \mathbf{L}_{F_i} by $\widehat{\Delta x_i}$ w.r.t the full remaining insertion depth (Δy_i). The point \mathbf{L}_{F_i} refers to the intersection between the line $(\mathbf{B}_i\mathbf{N}_i)$ and the horizontal line defined at the final insertion depth where point \mathbf{T}_i is located.

The objective of our steering algorithm is to calculate the optimal steering angle φ_i so as to be able to position the predicted needle tip $\widehat{\mathbf{N}}_{F_i}$ on the target \mathbf{T}_i . Steering the needle by φ_i by moving the needle base from \mathbf{B}_{i-1} to \mathbf{B}_i will move the point \mathbf{L}_{F_i} horizontally towards the target \mathbf{T}_i and optimally position it at $\widehat{\Delta x_i}$ from \mathbf{T}_i . Consequently, if the needle is steered by φ_i and inserted towards \mathbf{T}_i , the needle deflection, estimated by $\widehat{\Delta x_i}$, will enable the needle tip to reach the target \mathbf{T}_i with minimal error.

Fig. 6.II shows an example where the predicted needle tip position $\widehat{\mathbf{N}}_{F_1}$ is not correctly superimposed on the targeted point $\mathbf{T}_{i=1}$. In such cases, the steering algorithm (Fig. 6.III) takes advantage of the interaction modeling to simulate the effects of a given steering angle into the proximal needle bases.

Namely, starting from the insertion step $i = 1$, where the needle tip is at \mathbf{N}_1 , the algorithm will propose to steer the needle by φ_1 . This is done by moving the needle base from \mathbf{B}_0 to \mathbf{B}_1 in such a way that the point \mathbf{L}_{F_1} is positioned at $\widehat{\Delta x_2}$ from \mathbf{T}_1 . If the needle is steered by φ_1 and inserted towards \mathbf{T}_1 , the needle

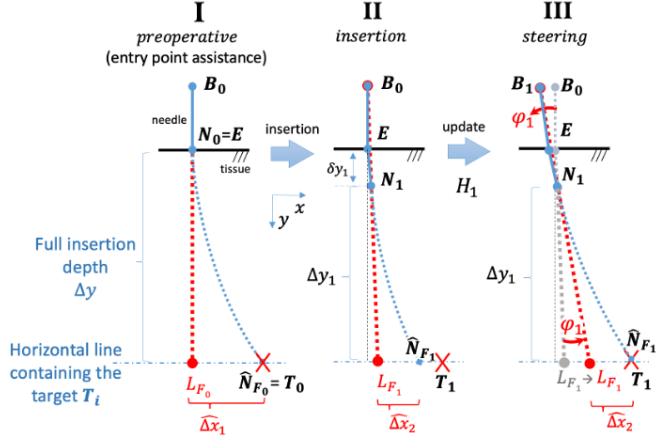


Figure 6: Detailed presentation of the proposed needle steering algorithm, including the steering angle $\varphi_i(\mathbf{B}_{i-1}, \mathbf{N}_i, \mathbf{B}_i)$ as system input (out of scale drawings showing the preop., insertion and steering steps for $i = 0, 1$). The inverse and direct deflection model supports needle position prediction $\widehat{\mathbf{N}}_{F_i}$ as well as updates of the adaptive parameter (H_i).

tip will reach \mathbf{T}_1 with minimal error.

Updating the needle base \mathbf{B}_i , needle tip \mathbf{N}_i and target \mathbf{T}_i positions, these iterations also apply to the subsequent steering-insertion steps until the full insertion depth (Δy).

The steering angle φ_i that provides the appropriate needle path correction so that $\widehat{\mathbf{N}}_{F_i} = \mathbf{T}_i$ can be calculated knowing the distance between the current position of $\mathbf{L}_{F_{i-1}}$ before steering and its desired position \mathbf{L}_{F_i} after steering as follows:

$$\varphi_i = \frac{\|\mathbf{L}_{F_i} - \mathbf{L}_{F_{i-1}}\|}{\Delta y_i}$$

where

$$\mathbf{L}_{F_{i-1}} = \mathbf{T}_i + \begin{bmatrix} -\widehat{\Delta x_i} \\ 0 \end{bmatrix}.$$

The estimated deflection value $\widehat{\Delta x_i}$ is obtained from the deflection model (Eq. (7)).

In the next section, experimental needle insertion procedures were performed using different robot platforms. Although our approach aims to be compatible with working under CT and MRI scenarios, for simplicity, a non CT/MRI-compatible experimental setup was used first to validate our approach at the lab level to avoid having to compete for access to the scarce clinical resources. This platform was based on a 2D video guidance and the Raven II platform [30].

Once the steering approach was validated under 2D video guidance with the Raven platform, *ex vivo* experimental results on 3D needle steering using the CT/MR-compatible LPR robot under CT-guidance were then presented.

3. Results

3.1. Experimental 2D Setup and Results on Needle Steering using the Raven II Robot

Experiment results involving robotic-driven needle steering assistance were obtained using 23 insertion samples in a synthetic phantom using the Raven II platform. The Raven II robot

was teleoperated (UDP protocol), with 7-Dof Sigma.7 (Force Dimension) serving as a haptic master device (Fig. 7). The Raven II was run with a Position-Position control loop at 1kHz. It can achieve sub-millimeter accuracy, as shown in [31]. The master and slave were in the same room and connected with a 2 m long ethernet cable. The measured teleoperation latency was ≤ 1 ms [32].

A graphical user interface (GUI) was developed to provide users with online image feedback and procedure data (target depth, current needle-target distance, needle trajectory, estimated error, etc.).

Two-dimensional images were acquired using a Toshiba Camileo Z100 digital video camera. Scenario measurements were obtained via accurate camera calibration using planar fiducial markers [33], with 9 px/mm resolution. The needle was visually detectable because the phantom tissues used were translucent. Thus, for every needle insertion step ($\approx 2\text{-}3$ cm per step), the needle tip position was tracked using a single mouse click on the developed interactive GUI. This manual tracking was a simple and quick task overall, as we worked with high resolution images (e.g. 1920x1080), and image zooms in the region of the mouse cursor.

Regarding the target definition, we assumed that the target was a virtual point defined by the user with a mouse click on the screen. In practice, target motion may be expected due to needle-tissue interactions. However, for simplicity, we considered that the target was stationary for this first steering validation. The long (20 cm) spinal 18G (Gauge) needle was inserted 23 times in different PVC phantoms mimicking different tissues as follows: 18 times in a) homogeneous phantom (100% soft PVC); 5 times in b) multi-layer phantom (5 layers): sponge, synthetic leather; extra soft PVC (80% soft PVC + 20% softener); 100% soft PVC; and 100% hard PVC. The multi-layer phantom was intended to mimic real non-homogeneous patient tissue layers.

The following video of the experiments provides a clear picture of the experimental workflow: www.youtube.com/watch?v=eZrKitZine8.

Needle insertions were performed under iterative time, *i.e.* progressively at regular intervals after the insertion steps. Each insertion step was around 30 mm depth. Users could update the current needle tip during the ≈ 5 s intervals provided for tissue relaxation. The needle tip position updates provided adaptive corrections for the previous needle deflection prediction. Needle steering was performed by manipulating the needle base according to the steering angle calculation and to the visual suggestions (based on augmented reality approaches) indicated in the GUI.

Needle insertion was performed at 60 mm/s speed and 50-100 mm depth range (see. Tab. 1). For the surface compression tests and tissue stiffness estimation, a 6-DoF force-torque sensor (nano43 from ATI Industrial Automation) was used only once preoperatively before starting the experiment. The intraoperative deflection estimation and steering guidance experiments were performed without using any force sensor data.

All the initial required parameters, such as tissue and needle

a) Homogeneous tissue			b) Heterogeneous tissue	
Exp. N°	Target location (final Insertion depth) (mm)	Targeting error (mm)	Target location (final Insertion depth) (mm)	Targeting error (mm)
1	65	0,0	109	1,0
2	80	0,5	104	0,5
3	85	0,7	119	1,4
4	85	0,2	115	0,5
5	85	0,2	112	1,0
6	85	0,2		
7	86	0,9		
8	83	0,9		
9	88	0,0		
10	80	0,7		
11	85	0,2		
12	78	1,2		
13	87	1,0		
14	93	0,2		
15	93	0,9		
16	90	1,7		
17	92	0,2		
18	93	0,2		
average (mm)	85,17	0,55	111,86	0,88
std (mm)	6,81	0,47	5,53	0,38

Table 1: Detailed results of needle insertion and steering approach for different target locations: a) 18 insertions into homogeneous tissues and b) 5 insertions into multi-layered heterogeneous tissue.

properties were obtained once preoperatively without any further update. Tissue stiffness K_t was preoperatively estimated by an axial compression test at the tissue surface level, as in [12], with coefficients $K_{t(Homog)} = 490$ N/m and $K_{t(Multilayer)} = 130$ N/m .

Hereafter we present the pHRI results for needle steering obtained using the above method. Fig. 7.III shows images of a real example of insertion with needle steering assistance in homogeneous PVC tissue.

Once the virtual target is defined (see Fig. 7.III.A), the tissue entry point suggestion is provided, followed by offline preliminary path prediction (Fig. 7.III.B). Then an insertion and needle tip update loop (Fig. 7.III.C-D) allows the system to provide steering assistance (Fig. 7.III.E). When applicable, the needle path correction is performed by lateral needle-base motion (Fig. 7.III.F). The procedure ends when the needle tip is at the same depth as the target (Fig. 7.III.H).

The deflection prediction model could be combined with the needle steering algorithm to provide steering assistance enhanced by online model updates. The user was provided intraoperative steering assistance, while taking the parameter uncertainties into account.

The robustness of the proposed adaptive model and the steering algorithm are illustrated in Fig. 8.

Fig. 8 and Tab. 1 illustrate a mean targeting error of 0.55 ± 0.4 mm for the homogeneous PVC tissue and 0.88 ± 0.3 mm for the heterogeneous phantom tissue. For the steering experiments, the needle was inserted at a mean depth ≈ 85 mm for the homogeneous tissue and ≈ 111 mm for the multi-layered het-

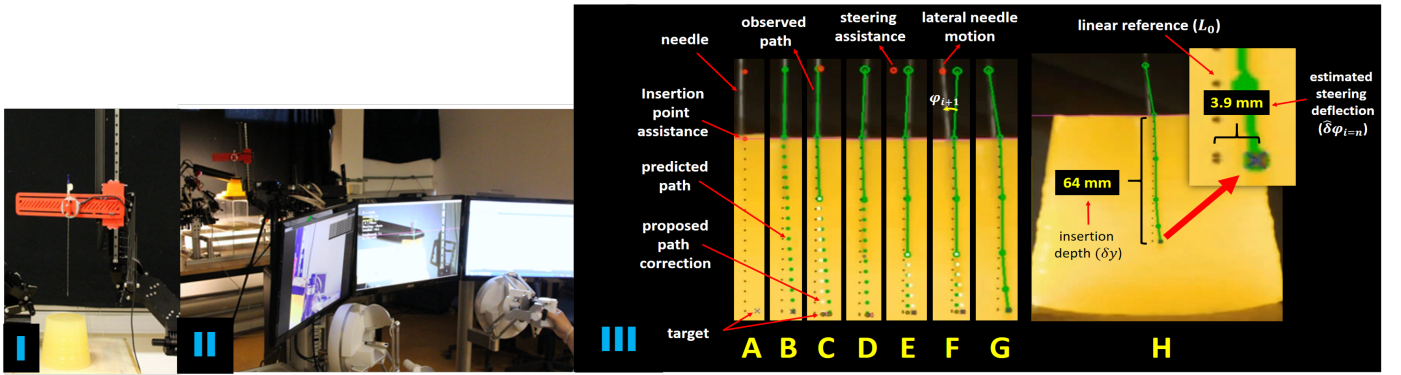


Figure 7: Raven II platform (I) customized to perform teleoperated needle insertion procedures (II). Needle steering guidance with lateral needle-base motion (III). Zoom detailing the user visual feedback of the needle path towards the target direction.

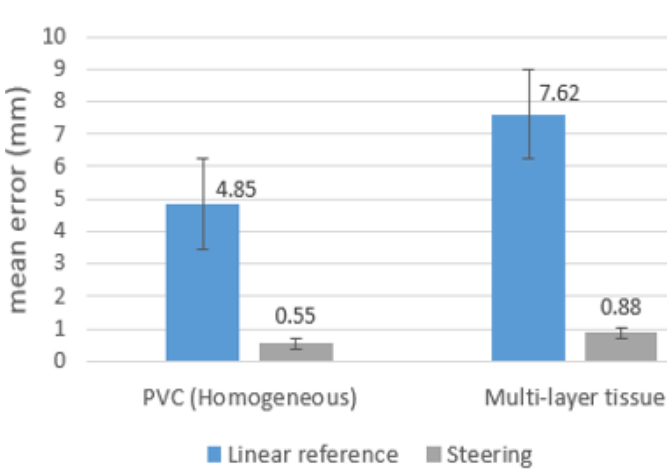


Figure 8: Results of needle steering approach compared to linear-based clinical reference.

erogeneous tissue. The needle tip deviation was measured up to 10 mm relative to a linear reference, *i.e.* where the needle is inserted straight without any steering. Tab. 1 details the obtained results for each needle insertion and steering for different target locations.

The robustness of our steering approach was also confirmed by minor variations (≤ 0.4 mm) in the standard deviation. Moreover, a comparison of inter-tissue errors revealed that it was very stable. Finally, a comparison of mean targeting errors of previous studies (*i.e.* 1.4 mm) [27] relative to offline predictions (without steering corrections) using Raven II highlighted the efficacy of the proposed steering algorithm in decreasing the targeting errors to submillimetric levels, as discussed above.

The experimental results confirmed the accuracy of the proposed pHRI model and the robustness of the targeting strategy when combined with the needle steering process and using the Raven II robot. Based on these encouraging experimental results, we programmed and performed *ex vivo* validation experiments with the LPR robot.

Since the LPR robot and our proposed pHRI model and steer-

ing are CT and MRI- compatible, the experimental validation could be readily performed under CT or MRI-guidance. Unfortunately, we do not have an MRI for research in our institution and we have no access to clinical MRI scanners. We thus performed the *ex vivo* validation under CT-guidance, as detailed hereafter.

3.2. Experimental Results on 3D Needle Steering using the LPR Robot

The needle steering algorithm was tested using LPR in a non-homogenous *ex vivo* pork tissue. The experiments were designed as follows:

- The tissue characteristics were obtained preoperatively before starting the experiment using the LASTIC platform [34]. LASTIC is a light aspiration device for *in vivo* soft tissue characterization. This system applies a range of negative pressures on the soft tissue and measures the resulting tissue deformations with a miniature camera. The tissue elasticity parameters can be estimated by combining these measurements with FEM modelling. This system was used rather than the force sensor to estimate the surface tissue properties. This enabled us to determine the 0.21 GPa value for K_t .
- A screw nut (5 mm dia.), simulating the physical target, was placed inside the *ex vivo* pork tissue through a path orthogonal to the penetration direction. It was used as a physical target during the experiments and was located nearly 87 mm from the tissue surface.
- Two different needles were tested. First, we used a standard 18G needle. The second one was a 20G stainless steel needle with a 38° beveled tip and a 0.9 mm outer diameter. As the needle was compact, the inner diameter was set at zero. Three full needle insertion experiments were performed using *ex vivo* pork tissue, where the adaptive insertion planning with steering and tissue entry point guidance were implemented. In addition, free insertion was performed without any assistance so as to be able to monitor and compare the findings of real needle deflection experiments with assisted needle insertion

experiments. One insertion was done using a standard 18G needle and two insertions were performed using a 20G needle which is thinner and more flexible than the 18G.

- d) Robotized insertion experiments were performed under the CT-guided scenario. CT image data were interpolated over the scanned workspace volume. Slice views of the orthogonal axial and sagittal planes provided 3D feedback of the scenario (Fig. 9.A). Since any point in the 3D space may be projected in both 2D orthogonal planes, the system was able to provide steering assistance in any direction. The final 3D error ε was thus also obtained by Eq. (9) based on the Euclidean distance between the needle-targeting errors observed for both axial and sagittal 2D planes.

$$\varepsilon = \sqrt{(N_{x_{\text{axial}}} - T_{x_{\text{axial}}})^2 + (N_y - T_y)^2 + (N_{z_{\text{sagittal}}} - T_{z_{\text{sagittal}}})^2} \quad (9)$$

$N = (N_{x_{\text{axial}}}, N_y, N_{z_{\text{sagittal}}})$ is the needle position measured at the same insertion depth (same y -axis) as the targeted point T . This latter was selected by the user at the center of the target surface. Since the relative needle-tip position was observed at the same insertion depth (*i.e.* needle insertion stop-criteria), we assume $N_y = T_y$.

The steering algorithm used 5 px/mm voxel resolution obtained from DICOM images to estimate the object dimensions located in the scene, while providing the user with steering assistance.

When the whole needle shaft and tissue were present in the same image slice (as in Fig. 9.A), the algorithm was able to provide steering assistance using relative needle-base positioning in each GUI plane.

As we were working in a 3D scenario, we often could not see the whole needle shaft at the same time, as the needle is usually distributed through several parallel slices. Augmented reality (AR) techniques were implemented in GUI to overcome this problem while still being able to identify the main objects in the image. Then the steering algorithm could identify, for each 2D slice, the positions of needle elements (needle fiducials) even when they were not visible in the current GUI windows. Fig. 9.B depicts several axial slices showing the needle fiducials such as the needle base B , needle entry point E , intermediate and current the needle tip positions N_i and the physical target T .

Figures 9.B.I-III show the main fiducials (*i.e.* needle base, entry point, current needle tip and target) relative to the time i on the different planes. Fig. 9.B.IV refers to the time $i + 1$ and shows GUI with the main steering parameters and AR resources being used to plot all of them on the same plane, despite the 2D image slice in the background.

Tab. 2 shows the obtained experimental targeting errors after the final needle insertion step. T is the target position preoperatively defined by the user (gold standard) and N is the measured needle tip position. The axial and sagittal components of $T - N$ and its norm ε (3D error Eq. (9)) are

Sample	needle	error (mm) (axial plane)	error (mm) (sagittal plane)	3D error (mm)
1 (S)	18G	0.3	0.30	0.42
2 (S)	20G	0.3	0.67	0.73
3 (S)	20G	0	0.3	0.30
4 (L)	20G	2	11	11.18

Table 2: Targeting errors obtained in the experiments with steering assistance (S) with the LPR robot under 3D CT-guidance. The last row (L) refers to needle deflection relative to the linear reference during free (open-loop) insertion.

reported in Tab. 2.

The average value of the 3D Euclidean error ε for the three samples was 0.49 ± 0.22 mm. The last sample shown in the table (sample 4(L)) refers to the observed needle deflection considering a free open-loop insertion without steering. The findings of this experiment enabled us to quantify the needle deflection obtained with the current needle-tissue setup while considering the same insertion depth (87 mm). When inserting the 20G biopsy needle, we observed a needle deflection of around 11.18 mm relative to the linear referential. Compared to the three experiments where needle steering assistance was used, we succeeded in reducing the error by $> 95\%$. Note also that despite the experiment was run at the limit of the constraint condition $\delta x/\mathcal{L} < 0.1$, it was still able to converge the predictions with errors of ≤ 1 mm.

Regardless of the quality of the obtained targeting accuracy, the main contribution of our work is the method itself which does not use any force measurement compared to existing state-of-the-art methods. For the limit of our knowledge, there is no other force-sensor-free method described in the literature that can be compared with our proposed method. However, there exists other steering methods based on the interaction force measurement that may perform better in terms of targeting precision as summarized in Tab. 3.

4. Discussion

Here we have presented a novel CT and MRI-compatible modeling of the physical interaction between a robotized needle and the patient.

The robotic platform and pHRI model and steering algorithm were designed to overcome ferromagnetic issues while being compatible with reduced workspaces inside the bore [25], [10]. The proposed model does not use the interaction force measurement as commonly proposed in the literature [11], [12], [19], [13], [20], [14]. This model is based only on the needle kinematics and kinetic studies using a phenomenological approach.

The findings of the CT-guided 3D steering experiments demonstrated the feasibility of the approach under *in vitro* and *ex vivo* needle insertion conditions. While the whole approach was also designed to be compatible with MRI-guided scenarios, we did not have access to a research-oriented MRI platform

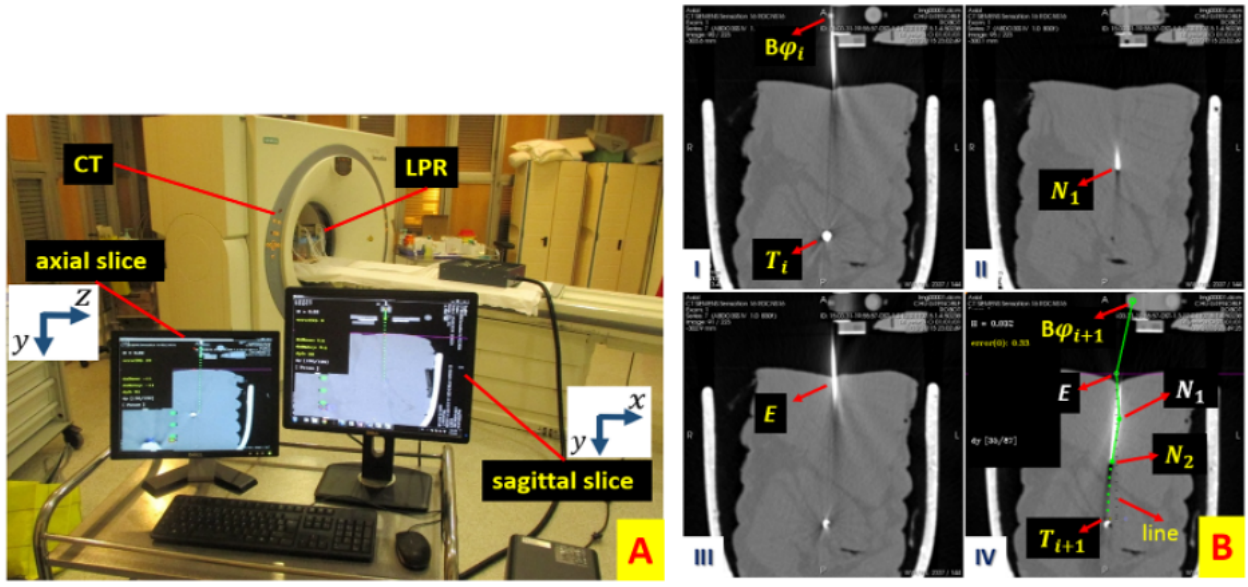


Figure 9: A. 3D needle steering using the LPR robot under CT-guidance. Axial and sagittal slices showing the needle position and intraoperative needle steering guidance. B. Interactive GUI with AR-based resources. The whole needle shaft was not entirely visible in every slice. (I-III) AR-based guidance (IV) improved visual feedback: all needle fiducials were assembled on the same image. GUI also provided feedback regarding the system parameters.

to validate our solution. However, since our proposed pHRI model and steering solution have been designed to be CT and MRI compatible and were experimentally validated *ex vivo* under CT-guidance, it may be assumed that they could be applicable to MRI-guided platforms.

Indeed, the MR-compatibility of our method is guaranteed by the MR-compatible mechatronics design of the used LPR robot and by the algorithmic part of our proposed modeling and steering method that is based only on the acquired image. However, considering the needle clearly visible in the MR image as shown in [5], the expected targeting precision of our proposed approach under MRI-guidance will be highly dependent on the quality and the resolution of the acquired MR image. MRI related experiments need to be conducted to fully validate the applicability of our proposed method under MRI-guidance.

The phenomenological-based techniques took the needle tip and target positions into account, along with the needle and tissue biomechanical properties.

Our original approach allowed us to predict the curved needle path by modeling the needle as articulated links and via low-cost computational processing. As our model is quite simple and linear, the algorithm does not necessitate much computational complexity and it can be computed almost instantaneously. It can thus provide instant updates for steering assistance and subsequent needle path prediction.

The resulting algorithms facilitate intraoperative adaptive insertion planning with needle steering and preoperative tissue entry point assistance.

Because of the simplicity of this needle steering solution, it could also be of potential interest for operations using 3D real-time image-guided percutaneous procedures, such as real-time MRI (which is very rare nowadays and is beyond the

scope of this work). Moreover, it might ultimately be possible to implement automatic needle tip tracking, which could be the focus of future studies.

These cross-platform robot-assisted experiments encountered issues not previously considered in the algorithms design, such as needle bending outside the tissue. During *in vitro* and *ex vivo* validation tests, the adaptive algorithm served as a failure contingency tool and could be automatically adapted for use in different robot platforms. The proposed algorithms are not platform specific and could function without any further experiments for (re)training or (re)tuning. The use of needle steering assistance reduced needle insertion error by $\approx 95\%$ compared to insertions using classical linear references.

Tab. 3 shows the main steering approaches that have been proposed in the literature to assist robot insertion. We have classified the studies according to the clinical target, needles and tissues used for the validation, insertion depth in the experiments, needle steering strategy, imaging feedback modality, type of deflection prediction (*i.e.* preoperative offline *vs.* intraoperative online), the compatibility of promising approaches with currently robotized needle insertion platforms (*e.g.* compatibility with MR imaging and rigid needles conventionally used in clinical routines), failure-contingency mechanism (adaptive compensation of the model to improve its performance online by overcoming scenario uncertainties), required demand for online data force input and reported mean error.

According to [24], 2-3 mm targeting errors could be acceptable for most surgical percutaneous procedures, as compared to the human manual targeting error [35], *i.e.* $\approx 3\text{-}5$ mm.

Therefore, the submillimeter targeting precision of most of these platforms validates their proposed control strategies. However, as presented in Tab. 3, the main challenges for robo-

Model	Target context	Needle type	Tissue	steering approach	feedback approach	depth (mm)	Prediction		MR-compatible semi-rigid needle	adaptive failure contingency	force measure input	claimed mean error (mm)
							pre	intra				
Wan, 2005 ³⁸	brachy-therapy	rigid rod (stainless steel)	ex-vivo (chicken)	axial/spin rotation	US	60	X				sensor	2.8
Rucker, 2013 ³²	abdomino-pelvic (liver*)	flexible (nitinol)	a) deformable phantom; b) ex-vivo bovine liver	axial/spin rotation	magnetic tracking	a) 85 b) 100		X			sensor	a) 0.5 b) 0.4
Moreira, 2014 ³⁰	neurosurg, brachy-therapy (*)	flexible (nitinol)	a) 2-layer gelatin; b) ex-vivo (chicken); c) ex-vivo + target mov	axial/spin rotation	US	90	X	X			sensor	a) 0.42 b) 1.56 c) 1.63
DiMaio, 2003 ⁸	brachy-therapy*	semi-rigid (stainless steel)	soft PVC stiffness variations: a) 15%; b) 50%	lateral movement	video	n/a		X	X		sensor	a) 1.0 b) 2.5
Kobayashi, 2009 ²³	abdomino-pelvic (liver)	rigid rod* (stainless steel)	deformable liver model	n/a	US	60*	X	X	X		sensor	1.5
Glozman, 2007 ¹³	laparosc.	semi-rigid (stainless steel)	a) ex-vivo (turkey); b) ex-vivo (beef);	lateral movement	fluorosc.	40	X	X	X		sensor	0.5
Our model	abdomino-pelvic (kidney)	semi-rigid (stainless steel)	a) soft PVC (homog); b) multi-layer phantom; c) ex-vivo pork	lateral movement	CT; video	50-100	X	X	X	X	free	a) 0.55 b) 0.88 c) 0.49

Table 3: Main steering and needle deflection prediction approaches proposed in the literature for different experimental conditions. Some information in the table was not directly available from the study. Therefore, when applicable, the information was deduced (*). When information was not applicable or not clearly available in the paper, it is indicated as (n/a).

tized needle steering assistance go beyond the targeting precision. Indeed, it's very challenging to compare different robotized steering approaches as they are assessed under rather different conditions/challenges and are highly dependent on the used robot and imaging feedback. The objective of Tab. 3 is not to compare the targeting performance of the proposed models. We want to emphasize through this analysis that the main contribution of our work is not the obtained precision but the method itself that does not use any force measurement and is thus CT/MRI compatible and safe. This contributes to answer to the safety challenges in the physical humanrobot interaction domain.

Moreover, the choice of using either flexible (nitinol) or rigid needles could limit the feasibility of the applications to existing robot platforms under given scenarios. Likewise, selecting one model over another may limit online deflection estimations to the use of CT/MR-compatible force sensors. The issues mentioned above hamper or complicate the use of many of these models under MRI robotized needle insertion procedures. The results obtained in this study thus revealed the potential of our proposed method to fill this gap.

5. Conclusion

In this work, we have proposed and experimentally validated an image-based interaction model compatible with both CT and MRI constrains and clinical scenarios. The method does not use any force measurement and is thus CT/MRI compatible and safe. This contributes to answer to the safety challenges in the physical humanrobot interaction domain. Future research could deal with further challenges under real scenarios using MRI-guidance, such as target motion, needle real-time tracking, obstacle deviation, alongside the use of elastography

to provide the model with pre/intraoperative tissue stiffness parameters.

Acknowledgments

This research was supported by the TECSAN ROBACUS project, granted by ANR (*French Agence Nationale de la Recherche*): ANR-11-TECS-020-01.

- [1] H. Su, A. Di Lallo, R. Murphy, R. Taylor, B. Garibaldi, A. Krieger, Physical humanrobot interaction for clinical care in infectious environments, *Nature Machine Intelligence* 3 (2021) 184–186. doi:10.1038/s42256-021-00324-z.
- [2] G. Kronreif, M. Frst, J. Kettenbach, M. Figl, R. Hanel, Robotic guidance for percutaneous interventions, *Advanced Robotics* 17 (2003) 541–560. doi:10.1163/15685530360675532.
- [3] B. Maurin, B. Bayle, O. Piccin, J. Gangloff, M. d. Mathelin, C. Doignon, P. Zanne, A. Gangi, A patient-mounted robotic platform for ct-scan guided procedures, *IEEE Transactions on Biomedical Engineering* 55 (10) (2008) 2417–2425. doi:10.1109/TBME.2008.919882.
- [4] D. Stoianovici, K. Cleary, A. Patriciu, D. Mazilu, A. Stanimir, N. Craciunoiu, V. Watson, L. Kavoussi, Acubot: a robot for radiological interventions, *IEEE Transactions on Robotics and Automation* 19 (5) (2003) 927–930. doi:10.1109/TRA.2003.817072.
- [5] P. Moreira, L. Kuil, P. Dias, R. Borra, S. Misra, Tele-operated mri-guided needle insertion for prostate interventions, *Journal of medical robotics research* 3 (4) (2018) 1842003. doi:10.1142/S2424905X18420035.
- [6] M. Abayazid, C. Pacchierotti, P. Moreira, R. Alterovitz, D. Prattichizzo, S. Misra, Experimental evaluation of comanipulated ultrasoundguided flexible needle steering, *The international journal of medical robotics + computer assisted surgery : MRCAS* 12. doi:10.1002/rcs.1680.
- [7] H. Su, J. S. S. Arévalo, M. R. Makhdoomi, G. Ferrigno, E. D. Momi, Safety-enhanced human-robot interaction control of redundant robot for teleoperated minimally invasive surgery, *2018 IEEE International Conference on Robotics and Automation (ICRA)* (2018) 6611–6616.
- [8] Z. Du, Y. Liang, Z. Yan, L. Sun, W. Chen, Human-robot interaction control of a haptic master manipulator used in laparoscopic minimally invasive surgical robot system, *Mechanism and Machine Theory* 156 (2021) 104132. doi:<https://doi.org/10.1016/j.mechmachtheory.2020.104132>.

- [9] V. Groenhuis, F. Siepel, J. Veltman, S. Stramigioli, Design and characterization of stormram 4: an mri-compatible robotic system for breast biopsy, in: 2017 IEEE/RSJ International Conference on Intelligent Robots and Systems (IROS), IEEE, United States, 2017, pp. 928–933. doi:10.1109/IROS.2017.8202256.
- [10] N. Zemiti, I. Bricault, C. Fouard, B. Sanchez, P. Cinquin, Lpr: A ct and mr-compatible puncture robot to enhance accuracy and safety of image-guided interventions, Mechatronics, IEEE/ASME Transactions on 13 (2008) 306 – 315. doi:10.1109/TMECH.2008.924045.
- [11] S. P. DiMaio, S. E. Salcudean, Needle steering and model-based trajectory planning, in: R. E. Ellis, T. M. Peters (Eds.), Medical Image Computing and Computer-Assisted Intervention - MICCAI 2003, Springer Berlin Heidelberg, Berlin, Heidelberg, 2003, pp. 33–40.
- [12] D. Glozman, M. Shoham, Image-guided robotic flexible needle steering, Robotics, IEEE Transactions on 23 (2007) 459 – 467. doi:10.1109/TR.2007.898972.
- [13] R. III, J. S. Kim, N. Cowan, G. Chirikjian, A. Okamura, Nonholonomic modeling of needle steering, I. J. Robotic Res. 25 (2006) 509–525. doi:10.1007/s11552-006-004.
- [14] C. Backes, A. Okamura, Modeling of needle insertion forces for robot-assisted percutaneous therapy., Vol. 2, 2002, pp. 2085–2091. doi:10.1109/ROBOT.2002.1014848.
- [15] H. Kataoka, T. Washio, M. A. Audette, K. Mizuhara, A model for relations between needle deflection, force, and thickness on needle penetration, in: MICCAI, 2001.
- [16] S. Misra, K. Reed, B. Schafer, K. Ramesh, A. Okamura, Mechanics of flexible needles robotically steered through soft tissue, I. J. Robotic Res. 29 (2010) 1640–1660. doi:10.1177/0278364910369714.
- [17] M. Bernardes, Robot assisted steering of flexible needles for percutaneous procedures, Ph.D. thesis, University of Montpellier, Montpellier, France (2012).
- [18] O. Goksel, E. Dehghan, S. E. Salcudean, Modeling and simulation of flexible needles, Medical engineering & physics 31 (9) (2009) 10691078. doi:10.1016/j.medengphy.2009.07.007. URL <https://doi.org/10.1016/j.medengphy.2009.07.007>
- [19] Y. Kobayashi, A. Onishi, H. Watanabe, T. Hoshi, K. Kawamura, M. G. Fujie, Developing a planning method for straight needle insertion using probability-based condition where a puncture occurs, 2009 IEEE International Conference on Robotics and Automation (2009) 3482–3489.
- [20] P. Moreira, I. Peterlik, M. Herink, C. Duriez, S. Cotin, S. Misra, Modelling prostate deformation: SOFA versus experiments, Mechanical Engineering Research 3 (2). doi:10.5539/mer.v3n2p64. URL <https://doi.org/10.5539/mer.v3n2p64>
- [21] N. Abolhassani, R. Patel, Deflection of a flexible needle during insertion into soft tissue, in: 2006 International Conference of the IEEE Engineering in Medicine and Biology Society, 2006, pp. 3858–3861. doi:10.1109/IEMBS.2006.259519.
- [22] M. Khadem, B. Fallahi, C. Rossa, R. Sloboda, N. Usmani, M. Tavakoli, A mechanics-based model for simulation and control of flexible needle insertion in soft tissue, Vol. 2015, 2015. doi:10.1109/ICRA.2015.7139499.
- [23] R. Roesthuis, Y. van Veen, A. Jahya, S. Misra, Mechanics of needle-tissue interaction, in: International Conference on Intelligent Robots and Systems (IROS 2011), IEEE ROBOTICS AND AUTOMATION SOCIETY, 2011, pp. 2557–2563, 10.1109/IROS.2011.6094969 ; null ; Conference date: 25-09-2011 Through 30-09-2011. doi:10.1109/IROS.2011.6094969. URL <http://ewh.ieee.org/soc/ras/conf/CoSponsored/IROS/2011/IROS/www.iros2011.org/index.html>
- [24] D. Rucker, J. Das, H. Gilbert, P. Swaney, M. Miga, N. Sarkar, R. Webster, Sliding mode control of steerable needles, Robotics, IEEE Transactions on 29 (2013) 1289–1299. doi:10.1109/TR.2013.2271098.
- [25] E. A. G. Dorileô, N. Hungr, N. Zemiti, I. Bricault, C. Fouard, P. Poignet, A modular CT/MRI-guided Teleoperation Platform for Robot Assisted Punctures Planning, in: CARS: Computer Assisted Radiology and Surgery, Fukuoka, Japan, 2014.
- [26] E. A. G. Dorileô, N. Zemiti, P. Poignet, Needle Deflection Prediction Using Adaptive Slope Model, in: ICAR 2015 - 17th International Conference on Advanced Robotics, IEEE, Istanbul, Turkey, 2015, pp. 60–65. doi:10.1109/ICAR.2015.7251434. URL <https://hal-lirmm.ccsd.cnrs.fr/lirmm-01275351>
- [27] E. A. G. Dorileô, A. Albakri, N. Zemiti, P. Poignet, Simplified adaptive path planning for percutaneous needle insertions, in: ICRA: International Conference on Robotics and Automation, Seattle, WA, United States, 2015, pp. 1782–1788. doi:10.1109/ICRA.2015.7139429.
- [28] J. M. Gere, S. P. Timoshenko, Mechanics of Materials, Van Nostrand Reinhold Company, 1972.
- [29] S. P. Parker, McGraw-Hill Education, McGraw-hill dictionary of scientific and technical terms, 6th Edition, McGraw-Hill Professional, New York, NY, 2002.
- [30] B. Hannaford, J. Rosen, D. C. W. Friedman, H. H. I. King, P. Roan, L. Cheng, D. Glozman, J. Ma, S. N. Kosari, L. W. White, Raven-ii: An open platform for surgical robotics research, IEEE Transactions on Biomedical Engineering 60 (2013) 954–959.
- [31] H. Peng, X. Yang, Y. Su, B. Hannaford, Real-time data driven precision estimator for RAVEN-II surgical robot end effector position, CoRR abs/1910.06425. arXiv:1910.06425.
- [32] J.-y. Lee, S. Payandeh, L. Trajkovic, Performance evaluation of transport protocols for internet-based teleoperation systems.
- [33] S. Daftry, M. Maurer, A. Wendel, H. Bischof, Flexible and user-centric camera calibration using planar fiducial markers, in: British Machine Vision Conference, ., 2013, pp. 1–13, 2013 British Machine Vision Conference : BMVC 2013 ; Conference date: 09-09-2013 Through 13-09-2013.
- [34] P. Schiavone, E. Promayon, Y. Payan, Lastic: A light aspiration device for in vivo soft tissue characterization, in: F. Bello, S. Cotin (Eds.), Biomedical Simulation, Springer Berlin Heidelberg, Berlin, Heidelberg, 2010, pp. 1–10.
- [35] E. Boctor, M. Choti, E. Burdette, R. Iii, Three-dimensional ultrasound-guided robotic needle placement: An experimental evaluation, The international journal of medical robotics + computer assisted surgery : MR-CAS 4 (2008) 180–91. doi:10.1002/rcs.184.